Polymers for Advanced Technologies

WILEY

polymers advanced technologies

RESEARCH ARTICLE

Optimization of Curing Temperature for Epoxy/SiO_2/Glass Fiber Composite: Dual Enhancement of Mechanical Strength and Thermal Stability for Thin-Walled Pressure Vessels

Asad Meer[1] | Bilal Islam[2,3,4] | Nabeel Maqsood[4,5] | Ahmad Nawaz[2,3] | Waseem Akram[6] | Malik Daniyal Zaheer[7] | Syed Nasir Shah[8] | Kateřina Skotnicová[5] | Israr Ud Din[9,10]

[1]Department of Mechanical Engineering, Faculty of Mechanical and Aeronautical Engineering, University of Engineering & Technology Taxila, Rawalpindi, Pakistan | [2]National Center for Physics, Quaid. i. Azam University Campus, Islamabad, Pakistan | [3]Department of Mechanical Engineering, University of Engineering & Technology Peshawar, Peshawar, Pakistan | [4]Department of Laser Technologies, Center for Physical Sciences and Technology, Vilnius, Lithuania | [5]Faculty of Materials Science and Technology, VSB – Technical University of Ostrava, Ostrava, Czech Republic | [6]College of Electronics and Information Engineering, Shenzhen University, Shenzhen, People's Republic of China | [7]Institute of Mechatronics, Kaunas University of Technology, Kaunas, Lithuania | [8]Department of Energy Engineering, Faculty of Mechanical and Aeronautical Engineering, University of Engineering & Technology Taxila, Rawalpindi, Pakistan | [9]Department of Aerospace Engineering, Khalifa University of Science & Technology, Abu Dhabi, UAE | [10]Brunel Composite Center (BCC), Brunel University of London, TWI Ltd., Great Abington, Cambridge, London, UK

Correspondence: Bilal Islam (bilal.islam@ftmc.lt) | Nabeel Maqsood (nabeel.maqsood@ftmc.lt)

Received: 29 July 2025 | **Revised:** 11 October 2025 | **Accepted:** 22 October 2025

Funding: This work was supported by the European Commission, CZ.10.03.01/00/22_003/0000048.

Keywords: optimal curing | polymer composite | silica-gel | thin pressure vessel | three phase composite

ABSTRACT

The development of advanced composite materials for thin-walled pressure vessels demands a balance between mechanical strength and thermal insulation. In this study, a novel three-phase composite system comprising epoxy resin, silica (SiO_2) micro-particles, and glass fiber reinforcement was fabricated and characterized for potential application in high-performance thin vessel structures. Specimens were cured at varying temperatures (60°C to 160°C) to systematically investigate the influence of curing conditions on the structural and thermal properties. Comprehensive material characterization, including Fourier transform infrared (FTIR) spectroscopy and x-ray diffraction (XRD) analysis, confirmed the successful integration of silica and glass fiber within the amorphous epoxy matrix. Thermogravimetric analysis (TGA) revealed a two-stage degradation process, with maximum thermal stability observed at 120°C curing temperature. Specific heat capacity (C_p) and measurements indicated decreasing trends with increasing curing temperature, enhancing thermal insulation. Mechanical testing demonstrated that hoop strength (S_H) and burst pressure (P_b) improved significantly with curing temperatures up to 140°C, following third-degree polynomial relationships. Notably, the composite cured at 120°C exhibited the highest combination of hoop strength (341.3 ± 6.5 MPa), burst pressure (16.66 ± 0.3 MPa), C_p (2.33 J/g·K), thermal conductivity (0.198 W/m·K) and Factor of Safety (1.39 ± 0.024), while maintaining superior thermal resistance. Theoretical predictions showed strong agreement with experimental results across all evaluations. Overall, the optimized epoxy/SiO_2/glass fiber composites

Abbreviations: λ, thermal conductivity; σ_1, maximum principal stress; σ_2, minimum principal stress; σ_{avg}, average normal stress; σ_{hoop}, hoop stress; σ_L, longitudinal stress; σ_{VM}, Von Mises equivalent stress; τ_{max}, maximum in-plane shear stress; $\tau_{max(in\text{-}plane)}$, maximum in-plane shear stress; $\tau_{max(out\text{-}plane)}$, maximum out-of-plane shear stress; C_p, specific heat capacity; FOS, factor of safety; FTIR, Fourier transform infrared spectroscopy; P_b, burst pressure; S_H, hoop strength; SiO_2, silica; TGA, thermogravimetric analysis; XRD, x-ray diffraction.

offer a lightweight, thermally stable, and mechanically robust alternative to traditional metallic vessels, highlighting their potential for use in chemical, oil, and pharmaceutical industries requiring durable thin-walled pressure containment solutions.

1 | Introduction

In recent years, there has been growing interest in the development of high-performance polymer composites designed to replace traditional metallic materials in a wide range of industrial applications. Among polymer matrices, epoxy resins have been extensively explored due to their excellent mechanical properties, superior chemical resistance, low shrinkage, strong adhesion, and easy processability. However, pure epoxy systems often exhibit certain limitations, including brittleness, low impact strength, and relatively high thermal conductivity compared to advanced composite structures. To overcome these drawbacks, researchers have increasingly focused on reinforcing epoxy matrices with inorganic fillers and fiber reinforcements to enhance their mechanical, thermal, and chemical properties [1, 2].

Several studies have demonstrated that the incorporation of ceramic fillers, such as zirconia (ZrO_2), titania (TiO_2), and silica (SiO_2), into epoxy matrices leads to significant improvements in the mechanical strength, thermal stability, and flame retardancy of composites [1, 3]. Similarly, the addition of fibrous reinforcements such as glass, carbon, or aramid fibers further augments the structural integrity and load-bearing capabilities of the matrix [4, 5]. Among these, glass fiber is particularly attractive due to its high tensile strength, cost-effectiveness, corrosion resistance, and favorable compatibility with epoxy resins.

While two-phase composites consisting of an epoxy matrix reinforced either with fibers or with fillers have been widely investigated and are already in commercial use, three-phase composites, integrating two distinct reinforcements (typically one fiber and one particulate filler), have only recently gained research attention [6]. These multi-phase systems offer the advantage of synergistic property enhancements by combining the mechanical strengthening effect of fibers with the thermal and chemical stability imparted by ceramic fillers. Silica (SiO_2) has emerged as a promising candidate for filler addition in epoxy-based systems, due to its intrinsic properties such as low thermal conductivity, high thermal stability, good dispersion characteristics, and excellent chemical inertness [7]. The addition of silica micro-particles not only enhances the composite's ability to withstand high operating temperatures but also reduces its thermal conductivity, making it highly suitable for applications where thermal insulation is critical. Uzay [8] studied three-phase KH550 and KH570 silane-coated SiO_2 nanoparticles reinforced with glass fibers and it was seen that DSC and TGA experimentations showed that salinized SiO_2 nanoparticles provided a better curing behavior and improved thermal stability for the composites. Recent research highlights the impact of curing parameters on epoxy-based hybrid composites for structural applications. For instance, Wen et al. demonstrated that optimizing cure temperature improves interfacial bonding and thermal conductivity in silica-filled epoxies [9]. Zheng et al. investigated cure kinetics using model-free isoconversional methods (KAS, Flynn-Wall-Ozawa) and reported a direct correlation between crosslink density and mechanical toughness [10]. Hawa et al. applied such optimization to glass-fiber pressure pipes and reported up to 20% improvement in burst strength at optimized curing schedules [11].

Recent work on glass-fiber/epoxy (GF/EP) laminates and pipes has mapped circumferential properties using split-disk or related tests and shown notable environmental degradation, but typically without systematic cure-temperature optimization or concurrent thermal property reporting (λ, C_p). Tănase et al. measured circumferential properties of GFRP pipes under aggressive media/temperature exposure, quantifying ~21% drops in UTS and modulus under alkaline conditions, yet did not resolve property optima versus cure temperature for thin-walled pressure designs [12]. In epoxy composites, matrix thermal conductivity is frequently reported near 0.20–0.36 $W \cdot m^{-1} \cdot K^{-1}$ depending on filler and processing; glass-derived particulate additions can even reduce λ relative to neat or differently filled epoxies (0.357 to 0.229 $W \cdot m^{-1} \cdot K^{-1}$ with increasing glass particulate content), underscoring the sensitivity of λ to microstructure rather than fiber content alone [13]. Mechanically, recent GRE/GFRP pipe studies emphasize aging, winding, or rubber-layer design not cure-temperature optima and often omit paired λ and C_p reporting needed for thermal management in pressure service [14, 15]. However, few studies systematically compare mechanical, thermal, and chemical properties across multiple cure temperatures for three-phase (epoxy/SiO_2/glass) composites, particularly in thin-walled pressure vessel design.

In industrial sectors such as oil and gas, pharmaceuticals, and aerospace, thin-walled pressure vessels and pipelines are exposed to a combination of high internal pressures and variable thermal environments. Traditionally, these pipes and vessels were fabricated from metals like steel and aluminum alloys. Although metals offer high mechanical strength, they suffer from issues like corrosion, heat loss due to high thermal conductivity, heavy weight, and susceptibility to fatigue and environmental degradation [6, 16–18]. These limitations often result in increased maintenance costs, operational inefficiencies, and reduced service life.

Composite materials, by contrast, offer significant advantages, including a high strength-to-weight ratio, corrosion resistance, and tailorable thermal properties, making them attractive alternatives for such demanding applications [6, 19]. Previous research has demonstrated the effectiveness of glass fiber-reinforced epoxy (GF/EP) composites in pipe applications for underground oil and gas transportation [20]. However, studies focusing on the integration of both glass fiber and silica into epoxy matrices for high-pressure, thermally stable pipe applications are extremely limited. Moreover, the effect of curing temperature on the final mechanical and thermal properties of such three-phase composites remains relatively underexplored. It is well established that the degree of crosslinking during epoxy curing plays a critical role in determining the composite's structural and thermal performance. Optimal curing conditions can enhance crosslink density, thereby improving strength and stability, while excessive curing can lead to thermal degradation and embrittlement [21, 22].

There is no comprehensive study that systematically investigates the mechanical and thermal characterization, including hoop strength, burst pressure, thermal conductivity, and specific heat capacity, of glass fiber/SiO_2/epoxy three-phase composites designed for thin-walled vessel applications, with a specific focus on curing temperature optimization.

The present research study aims to fabricate and characterize thin-walled vessel structures based on a novel three-phase composite system composed of epoxy matrix, glass fiber reinforcement, and silica micro-particles. A thorough experimental and theoretical evaluation is conducted, including Fourier transform infrared spectroscopy (FTIR), x-ray diffraction (XRD), thermogravimetric analysis (TGA), hoop strength testing, burst pressure measurements, thermal conductivity, and specific heat capacity determination across a range of curing temperatures. The final aim is to establish an optimal composite formulation and curing regime that maximizes mechanical strength and minimizes thermal conductivity, offering a viable alternative to conventional metal pipes in critical industrial applications.

2 | Material and Method

2.1 | Material

A bisphenol-A based diglycidyl ether epoxy resin (DGEBA, commercial grade ER-155) and a cycloaliphatic amine curing agent (CA-155) were procured from Polymers Industries (Pvt.) Ltd., Gujranwala, Pakistan. The epoxy resin exhibited a viscosity of 11–14 Pa·s at 25°C and a density of 1.15 g/cm^3, while the curing agent had a density of 0.95 g/cm^3. Both components were used in a resin-to-hardener weight ratio of 2:1, as recommended by the supplier. High-purity silica (SiO_2) powder (99.5%, Merck Chemicals) with an initial particle size distribution of 20–80 μm and a BET surface area of 75 m^2/g was used as the particulate filler. E-glass woven fiber mats (plain weave, areal density 165 g/m^2, thickness 0.25 mm, silane-sized for epoxy compatibility) were sourced from Jushi Group Co. Ltd. as the fibrous reinforcement. Additionally, 3-methoxypropyltrimethoxysilane (98% purity, Sigma-Aldrich) was used as a coupling agent for the surface treatment of silica particles.

2.2 | Glass Fiber Reinforcement

E-glass fibers in the form of woven mats (plain weave) were obtained from Jushi Group Co. Ltd. The mats had an areal density of 165 g/m^2, a thickness of 0.25 mm, and were pre-treated with a silane-based sizing compatible with epoxy resin to promote adhesion. For the filament winding process, continuous E-glass rovings (2400 tex) were used. These rovings were drawn directly from spools under controlled tension during winding to ensure consistent fiber placement and load-bearing capability. The E-glass fibers exhibited a tensile strength of 3.45 GPa, Young's modulus of 72 GPa, and density of 2.56 g/cm^3, as per supplier specifications.

Curing was carried out in a convection oven with forced-air circulation to maintain a uniform temperature (±2°C). The temperature ramp rate was 3°C/min from ambient to the set curing temperature, held for 2 h. Relative humidity during curing was uncontrolled but maintained below 50% RH. After curing, samples were cooled gradually inside the oven (2°C/min) to minimize residual stress, then demolded. All specimens were conditioned for 24 h at 23°C ± 2°C and 50% ± 5% RH before mechanical and thermal testing, in accordance with ASTM D618.

2.3 | Silica Surface Treatment

To improve interfacial bonding between silica and epoxy, the silica particles were treated with a 1% v/v methoxysilane solution prepared in ethanol. The silica was dispersed in the solution using an ultrasonic bath (40 kHz) for 20 min to achieve uniform suspension. The mixture was then mechanically stirred at 25°C for 30 min to facilitate silane adsorption onto the silica surface. Subsequently, the treated silica was oven-dried at 80°C for 1 h to remove residual solvent and complete the silanization reaction.

2.4 | Epoxy–Silica Mixture Preparation

The epoxy resin and curing agent were mixed in a 2:1 (w/w) ratio using a mechanical overhead stirrer at 500 rpm for 10 min to ensure homogeneous blending. Silanized silica particles (1 wt% relative to epoxy resin) were gradually added to the mixture while maintaining constant stirring at 500 rpm for an additional 15 min. The resulting resin–silica mixture was then degassed under vacuum at −0.09 MPa for 5 min in a vacuum chamber to remove entrapped air bubbles and prevent void formation during curing.

2.5 | Sample Preparation

For flat composite samples, a Teflon-coated mold was used to facilitate easy demolding and ensure a smooth surface finish. For pipe fabrication, a steel mandrel of length 500 mm and outer diameter 86 ± 0.1 mm was employed, coated with a polyvinyl alcohol (PVA)-based release agent to prevent adhesion. Glass fiber mats were hand-laminated and thoroughly impregnated with the resin–silica mixture, ensuring complete wetting of fibers and uniform distribution of the filler.

2.6 | Filament Winding of Pipes

Filament winding was performed on a numerically controlled (NC) filament winding machine. Fibers were wound at ±90° hoop orientation under a controlled tension, monitored via an integrated tension control system. The mandrel was rotated at lower revolutions per minute to synchronize with fiber payout speed, ensuring even winding and fiber alignment. Four sequential layers of fiber were applied to achieve the target wall thickness of 2.15 mm.

2.7 | Curing Process

The wound and molded composites were cured using a two-step thermal process. Pre-curing was conducted by heating the

samples from ambient temperature to the target curing temperature (60°C, 80°C, 100°C, 120°C, 140°C, or 160°C) at a controlled ramp rate of 2°C/min, followed by an isothermal hold for 4 h to achieve crosslinking. A subsequent post-curing step was performed by maintaining the same temperature for an additional 15 min to ensure complete polymerization. The samples were then allowed to cool naturally to room temperature (approximately 25°C) under ambient conditions.

2.8 | Characterization of Epoxy-Silica Composite

Comprehensive physicochemical characterization of the fabricated epoxy–silica composites was conducted to verify the successful incorporation of silica micro-particles and to assess the structural features of the final material.

Fourier Transform Infrared (FTIR) Spectroscopy was employed to identify the characteristic functional groups and to confirm the chemical interaction between the epoxy matrix and the silica filler. FTIR measurements were performed using a Paragon 500 FTIR spectrometer (PerkinElmer, USA), operating over a spectral range of 2.5 to 25 μm (equivalent to 4000–400 cm^{-1} wavenumber). Each spectrum was collected at room temperature under ambient conditions with sufficient resolution to detect subtle differences in bond formation and filler dispersion within the composite.

XRD analysis was carried out to investigate the crystalline and amorphous phases present in the composite samples. The diffraction patterns were recorded using an X'Pert Pro PANalytical diffractometer equipped with Cu Kα radiation ($\lambda = 1.5406$ Å), operating at an accelerating voltage of 40 kV and a current of 30 mA. Scans were performed over a 2θ range from 10° to 90° at a scan rate optimized to ensure a high signal-to-noise ratio and accurate peak identification. The diffraction data enabled the identification of silica-related phases and the evaluation of the overall amorphous nature of the epoxy matrix. Both FTIR and XRD analyses were instrumental in confirming the successful fabrication of the three-phase composite system, ensuring effective integration of the SiO_2 filler without introducing undesirable crystalline impurities or phase separations.

2.9 | Thermal Characterization

TGA was performed to evaluate the thermal stability and degradation behavior of the epoxy–silica composite specimens as a function of temperature. The measurements were conducted using a high-precision TGA instrument under a controlled inert atmosphere to prevent oxidative degradation during heating. Specimens with a mass ranging from 4 to 10 mg were carefully prepared to ensure consistency and minimize experimental variability. Each sample was heated at a constant rate of 2°C/min under nitrogen flow to resolve overlapping mass-loss steps [23] and minimize the possible effect of thermal lag [24] an approach which is very consistent with the International Confederation for Thermal Analysis and Calorimetry (ICTAC) recommendations and guidelines [25]. The weight loss (%) was continuously recorded as a function of increasing temperature. TGA analysis was performed using alumina pans, and nitrogen purge 50 mL min^{-1}. To minimize thermal lag and gas-diffusion artifacts, the sample mass was standardized to 8.0 ± 0.5 mg (flake geometry; layer < 1 mm), placed centrally in the pan. Heating rates for kinetic analysis were 5°C, 10°C, and 20°C min^{-1}. Raw signals were corrected for baseline/buoyancy and mass-normalized prior to derivative (DTG) computation. For quality control, runs falling outside 6–9 mg were excluded from kinetic fitting. The TGA curves were analyzed to determine the distinct stages of thermal degradation, residual mass, and thermal decomposition temperatures, providing critical insights into the composite's thermal endurance and filler-matrix interactions. The activation energy for thermal degradation was further estimated using model-free kinetic approaches, enhancing the understanding of thermal stability imparted by the addition of silica micro-particles. The weight loss can be mathematically calculated as follows [26]:

$$\alpha = \frac{W_i - W_T}{W_i - W_d} \tag{1}$$

where α, W_i, w_T, w_d are degradation constant, initial, specific temperature, and degraded weight of the sample, respectively. Furthermore, the activation energy (E_a) can be estimated by using TGA through the Kissinger-Akahira-Sunose (KAS) model as follows [27, 28]:

$$ln\left(\frac{\beta_i}{(T_{i,\alpha})^2}\right) = \ln\left(\frac{RA_\alpha}{E_a g(\alpha)}\right) - \frac{E_a}{RT_{\alpha,i}} \tag{2}$$

where β_i, $T_{i,\alpha}$, R, A, and $g(\alpha)$ are heating rate, corresponding temperature, gas constant, pre-exponential constants and curing constant function, respectively. E_a can be calculated by plotting $ln(\beta_i/(T_{i,\alpha})^2)$ against $T_{i,\alpha}$ on y- and x-axis effectively.

Specific heat capacity (C_p) was also determined using ASTM-E1269 by the under-mentioned relation [29]:

$$Cp(s) = Cp(st) \times \left(\frac{D_s \times W_{st}}{D_{st} \times W_s}\right) \tag{3}$$

$C_P(s)$ [J/(g·K)] is the specific heat capacity of test sample, C_P(st) [J/(g·K)] shows specific heat capacity of sapphire standard, D_s (mW) shows peak heat absorbed by the test specimen using dynamic scanning calorimetry (DSC). Moreover, D_{st} (mW) is the maximum heat absorbed by the sapphire standard specimen at a given temperature. Similarly, W_s and W_{st} [mg] represent masses of the test and sapphire standard sample.

The thermal conductivity of the samples was also determined experimentally using ASTM E-1530. According to ASTM E-1530 a circular specimen was prepared with the diameter and thickness of 50.8 ± 0.25 and 2.0 ± 0.025 mm, respectively. Afterwards, the sample was subjected to a thermal conductivity meter (DTC-300) which measured thermal conductivity using the following relations [30]:

$$C_s = \frac{1}{R_s} \tag{4}$$

$$\frac{dQ}{dt} = C_s A dT \tag{5}$$

$$R_s = \frac{N(T_1 - T_2)}{Q} - R_o \tag{6}$$

$$\lambda = \frac{dx}{R_s} \tag{7}$$

C_s, R_s, A, dT, dQ/dT, dx, and λ are thermal conductance, thermal resistance, area of sample, temperature differential, heat flux and thermal conductivity, respectively. In addition, the terms N and R_o are temperature dependent fitting parameters.

3 | Theoretical Assumptions and Estimation

3.1 | Hoop Strength

The change in hoop strength with respect to curing temperature is assumed to be a non-linear second-order relationship dependent on curing temperature (T_{curing}) which can be written mathematically as:

$$\frac{\sigma_{hoop}}{dT_{curing}} = \left((C_1 T_{curing})^2 + C_2 T_{curing} + C_3 \right) \tag{8}$$

Taking integration of Equation (8)

$$\int d\sigma_{hoop} = C_1 \int (T_{curing})^2 dT_{curing} + C_2 \int T_{curing} dT_{curing} + C_3 \int dT_{curing} \tag{9}$$

$$\sigma_{hoop} = \left(\frac{k_o\, \sigma_{hoop(min)}}{T^3_{cur(min)}} \right) \frac{(T_{curing})^3}{3} + \left(\frac{k_1\, \sigma_{hoop(min)}}{T^2_{cur(min)}} \right) \frac{(T_{curing})^2}{2} + \left(\frac{k_2\, \sigma_{hoop(min)}}{T_{cur(min)}} \right) (T_{curing}) + k_3\, \sigma_{hoop(min)} \tag{10}$$

σ_{hoop} [MPa] depicts the hoop strength, T_{curing} [°C] represents curing temperature, $C_1 = (k_o \times \sigma_{hoop,(min)}/3(T_{cur(min)})^3)$, $C_2 = (k_1 \times \sigma_{hoop,(min)}/2(T_{cur(min)})^2)$, $C_3 = (k_2 \times \sigma_{hoop,(min)}/T_{cur(min)})$, and $C_4 = k_3 \times \sigma_{hoop(min)}$ are integration constants of the relation having units MPa/°C^3, MPa/°C^2, MPa/°C and MPa, respectively. Additionally, k_o, k_1, k_2, and k_3 are unit-less coefficients. Moreover, $\sigma_{hoop,(min)}$ and $Tc_{ur(min)}$ are constant minimum hoop strength ($\sigma_{hoop(min)}$) and minimum curing temperature $Tc_{ur(min)}$ depending on the orientation of the fiber, matrix material and filler quantity in the analysis.

3.2 | Burst Pressure

Change in burst pressure (dP_{burst}) with a changing curing temperature (dT_{curing}) is assumed to be a 2nd order relation dependent on curing temperature [see Equation (11)].

$$\frac{dP_{burst}}{dT_{curing}} = \left((C_1 T_{curing})^2 + C_2 T_{curing} + C_3 \right) \tag{11}$$

integrating both sides:

$$\int dP_{burst} = C_1 \int (T_{curing})^2 dT_{curing} + C_2 \int T_{curing} dT_{curing} + C_3 \int dT_{curing} \tag{12}$$

$$\int dP_{burst} = \left(\frac{B_o \times P_{burst(min)}}{T^3_{cur(min)}} \right) \frac{(T_{curing})^3}{3} + \left(\frac{B_1 \times P_{burst(min)}}{T^2_{cur(min)}} \right) \frac{(T_{curing})^2}{2} + \left(\frac{B_2 \times P_{burst(min)}}{T_{cur(min)}} \right) (T_{curing}) + B_3 P_{burst(min)} \tag{13}$$

P_{burst} [MPa] is the burst pressure, T_{curing} [°C] represents curing temperature, and C_1, C_2, C_3, and C_4 are integration constants, further correlated with other parameters. $C_1 = (\beta_o \times P_{Burst(min)}/3(T_{cur(min)})^3)$, $C_2 = (\beta_1 \times P_{Burst(min)}/2(T_{cur(min)})^2)$, $C_3 = (\beta_2 \times P_{Burst(min)}/(T_{cur(min)}))$, and $C_4 = \beta_3 \times P_{Burst(min)}$. Moreover, B_o, B_1, B_2, and B_3 are dimensionless coefficients. Similarly, the corresponding, $P_{Burst(min)}$ and $T_{cur(min)}$ are the minimum burst pressure and curing temperature.

3.3 | Factor of Safety

Variation in factor of safety (FOS) with respect to changing curing temperature is also considered to be a non-linear second-order curing temperature-dependent polynomial. The mathematical representation is as follows:

$$\frac{dFOS}{dT_{curing}} = \left((C_1 T_{curing})^2 + C_2 T_{curing} + C_3 \right) \tag{14}$$

Taking integral on both sides of Equation (14)

$$\int \frac{dFOS}{dT_{curing}} = C_1 \int (T_{curing})^2 dT_{curing} + C_2 \int T_{curing} dT_{curing} + C_3 \int dT_{curing} \tag{15}$$

Integration constants (i.e., C_1, C_2, C_3, and C_4) are further correlated with other parameters (i.e., $C_1 = (A_o/3(T_{cur(min)})^3)$, $C_2 = (A_1/2(T_{cur(min)})^2)$, $C_3 = (A_2/(T_{cur(min)}))$, and $C_4 = A_3 \times T_{cur(min)}$) and are substituted in Equation (15)

$$FOS = \left(\frac{A_o}{T^3_{cur(min)}} \right) \frac{(T_{curing})^3}{3} + \left(\frac{A_1}{T^2_{cur(min)}} \right) \frac{(T_{curing})^2}{2} + \left(\frac{A_2}{T_{cur(min)}} \right) (T_{curing}) + (A_3 \times T_{cur(min)}) \left(\frac{1}{T_{min}} \right) \tag{16}$$

where A_o, A_1, A_2, and A_3 are unitless constants of the above-mentioned relation.

3.4 | Specific Heat Capacity

Change in specific heat capacity with respect to curing temperature is assumed to be a first-order linear relationship, written as:

$$\frac{dC_p}{dT_{Sample}} = \left(C_1 T_{Sample} + C_2 \right) \tag{17}$$

Taking integration of Equation (17)

$$\int \frac{dC_p}{dT_{Sample}} = \int \left(C_1 T_{Sample} + C_2 \right) dT_{Sample} \tag{18}$$

These integration constants, that is, C_1, C_2, and C_3 are further correlated as $C_1 = D_o/2(T_{\text{Sample, (min)}})^2$, $C_2 = D_1/(T_{\text{Sample, (min)}})$, and $C_3 = D_2 \times C_p$ accordingly. By substituting with co-relation, the final expression becomes:

$$C_p = \left(\frac{D_o}{T^2_{\text{Sample(min)}}}\right)\frac{(T_{\text{Sample}})^2}{2} + \left(\frac{D_1}{T_{\text{Sample(min)}}}\right)(T_{\text{Sample}}) + D_2 \times C_p \tag{19}$$

3.5 | Thermal Conductivity

Variation in thermal conductivity with respect to changing sample temperature (T_{Sample}) is assumed to be linear, written as:

Whereas,

$$\frac{d\lambda}{dT_{\text{Sample}}} = (C_1 T_{\text{Sample}} + C_2) \tag{20}$$

Taking integration of Equation (20)

$$\int d\lambda = C_1 \int T_{\text{Sample}} dT_{\text{Sample}} + C_2 \int dT_{\text{Sample}} \tag{21}$$

Integration constants (i.e., C_1, C_2, and C_3) are given as: $C_1 = H_o \times \lambda_{\min}/2(T_{\text{Sample,(min)}})^2$, $C_2 = H_1 \times \lambda_{\min}/(T_{\text{Sample,(min)}})$, and $C_3 = H_2 \times \lambda_{\min}$. By substituting integration constants with their equivalents, the final mathematical expression becomes:

$$\lambda = \left(\frac{H_o \times \lambda_{\min}}{T^2_{\text{Sample(min)}}}\right)\frac{(T_{\text{Sample}})^2}{2} + \left(\frac{H_1 \times \lambda_{\min}}{T_{\text{Sample(min)}}}\right)(T_{\text{Sample}}) + H_2 \times \lambda_{\min} \tag{22}$$

λ [W/m·K] is the thermal conductivity, T_{Sample} [K] represents the temperature of the sample, $\lambda_{\min}$ is the minimum value of thermal conductivity, $T_{\text{Sample(min)}}$ is the minimum value of sample temperature and H_0, H_1, and H_2, are fitting parameters of the relation.

4 | Theoretical Design Formulation

The thin vessel/pipe with an inner radius and wall thickness of 43.00 and 2.15 mm, respectively, can withstand 10 MPa. Hence, to confirm designing the vessel requires estimation of hoop stress (σ_H), longitudinal stress (σ_L), maximum in-plane shear stress ($\tau_{\text{max(in-plane)}}$), and maximum out-of-plane shear stress ($\tau_{\text{max(out-plane)}}$), which are approximately incurred by the vessel accordingly. Hence, these parameters are approximated using the under-mentioned equations [31]:

$$\sigma_H = \left(\frac{P_g r}{t}\right) \tag{23}$$

$$\sigma_L = \left(\frac{P_g r}{2t}\right) \tag{24}$$

$$\tau_{\max(\text{in-plane})} = \left(\frac{P_g r}{4t}\right) \tag{25}$$

$$\tau_{\max(\text{out-plane})} = \left(\frac{P_g r}{2t}\right) \tag{26}$$

Consider a two-dimensional infinitesimal square shaped element from this pipe/vessel, as well as longitudinal and hoop stresses applied to the element, which are equivalent to normal stresses in the x and y axes. Furthermore, based on the two-dimensional plane stress condition, the Mohr circle was created using the calculated parameters (i.e., mean or nominal stress (σ_{avg}), maximum stress Tresca criteria (τ_{max}), principal stresses (σ_1 and σ_2), rotation angles of principal normal stresses plane/s (Θ_{p1} and Θ_{p2}), rotation angles of principal normal stresses plane/s (Θ_{s1} and Θ_{s2}), Tresca yield stress (σ_{YT}) and Von-Mises stress (σ_{VM}) sequentially). Mathematically, these parameters are computed as [32]:

$$\sigma_{avg} = \left(\frac{\sigma_x + \sigma_y}{2}\right) \tag{27}$$

$$\tau_{max} = \sqrt{\left(\frac{\sigma_x + \sigma_y}{2}\right)^2 + \tau_{xy}^2} \tag{28}$$

$$\sigma_1 = \sigma_{avg} + \tau_{max} \tag{29}$$

$$\sigma_2 = \sigma_{avg} - \tau_{max} \tag{30}$$

$$\sigma_{Y(T)} = \sigma_1 - \sigma_2 \tag{31}$$

$$\sigma_{VM} = \sqrt{\frac{(\sigma_1 - \sigma_2)^2 + (\sigma_2)^2 + (-\sigma_1)^2}{2}} \tag{32}$$

$$\theta_{p1} = 90^o + \theta_{p2} \tag{33}$$

$$\theta_{p2} = \frac{\tan^{-1}\left(\frac{2\tau_{xy}}{\sigma_x - \sigma_y}\right)}{2} \tag{34}$$

$$\theta_{s1} = 90^o + \theta_{s2} \tag{35}$$

$$\theta_{s2} = \frac{\tan^{-1}\left(\frac{-(\sigma_x - \sigma_y)}{2\tau_{xy}}\right)}{2} \tag{36}$$

5 | Results and Discussion

5.1 | Theoretical Design Approximations

Theoretical stress analyses were conducted to evaluate the mechanical loading conditions that the fabricated composite vessels would experience under internal pressure. Using Equations (23–25), hoop stress (σ_H), longitudinal stress (σ_L), and maximum out-of-plane shear stress ($\tau_{\text{max(out-plane)}}$) were calculated under an applied internal gauge pressure of 10 MPa. The corresponding values were determined as 200, 100, and 100 MPa, respectively. To visualize and further analyze the stress states, a Mohr's circle was constructed, graphically representing the principal stresses, maximum shear stresses, and angular orientation of stress planes. From the Mohr's circle analysis average normal stress (σ_{avg}) of 150.0 MPa, maximum

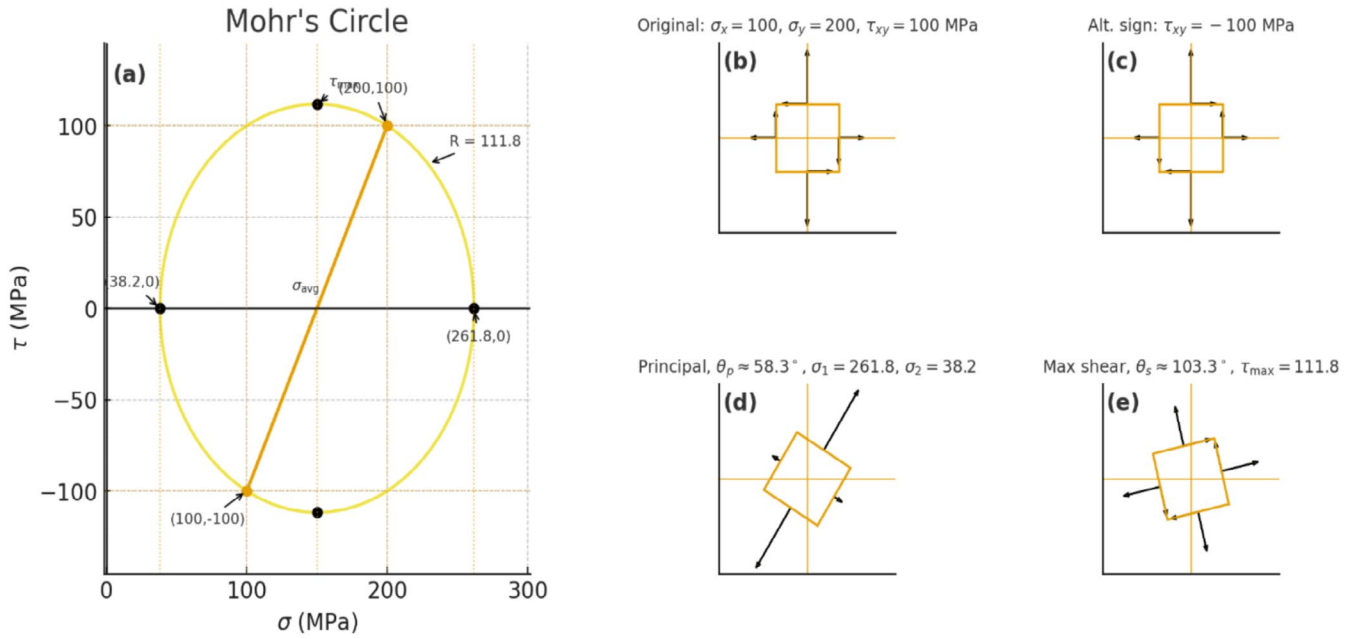

FIGURE 1 | (a) 2D Mohr circle for infinitesimal element of vessel (b) un-rotated element (c) rotated at 0° (d) rotated to τ_{max} (e) rotated to σ_1.

principal stress (σ_1) of 261.8 MPa, minimum principal stress (σ_2) of 38.2 MPa and maximum in-plane shear stress (τ_{max}) of 111.8 MPa were extracted. These values are illustrated in Figure 1 and are consistent with the calculations based on Equations (27–30). Further, using Equations (31) and (32), the maximum principal stress (σ_1) and the von Mises equivalent stress (σ_{VM}) were estimated as 261.8 and 244.94 MPa, respectively. The rotation angles associated with the orientation of the principal planes were also computed. Principal normal stress plane angles (Θ_{p1} and Θ_{p2}) of 58.238° and −31.717°, respectively, and maximum shear stress plane angles (Θ_{s1} and Θ_{s2}) of 103.283° and 13.283°, respectively were computed. These angular measurements indicate the orientations at which the vessel material experiences either maximum normal stresses or maximum shear stresses under operational loading conditions. Importantly, this theoretical analysis highlights a critical design criterion: the σ_H of the composite material must exceed the σ_{VM} under the given loading conditions to prevent structural failure. Ensuring that $\sigma_H > \sigma_{VM}$ provides a sufficient safety margin against yielding or catastrophic rupture, particularly in pressure vessel applications where multi-axial stresses are predominant.

5.2 | FTIR

FTIR Spectroscopy was conducted to analyze the chemical structure of the fabricated epoxy–silica composites and confirm the successful incorporation and interaction of silica, epoxy resin, and curing agents. The spectral measurements were obtained in the wavenumber range of 4000–400 cm^{-1}, capturing the full vibrational fingerprint region relevant to both organic and inorganic constituents. Composite samples cured at different temperatures 60°C, 80°C, 100°C, 120°C, 140°C, and 160°C were examined. Their corresponding FTIR spectra are presented in Figure 2a–f, illustrating consistent trends and peak shifts associated with functional group interactions across the curing temperature range. A prominent broad absorption band observed between 3200 and 3600 cm^{-1} corresponds to the O—H stretching vibrations of hydroxyl groups, which are commonly associated with the moisture content or unreacted hydroxyl groups in the epoxy network. Strong O—H peaks centered between 3546 and 3561 cm^{-1} were present in all samples, indicating retained hydroxyl functionality throughout the matrix. The presence of amine groups ($R—NH_3^+$) was confirmed by absorption bands in the range of 2122–2131 cm^{-1}, arising from the curing agent's contribution. These observations are consistent with prior findings, such as those reported by Nikolic et al. [33], where similar absorption bands were linked to amine cross-linkers in epoxy systems.

Key peaks between 1086 and 1093 cm^{-1} were attributed to the Si—O—Si asymmetric stretching vibrations, signifying the successful incorporation of silica particles into the matrix. Additionally, bands observed in the 971–984 cm^{-1} range correspond to Si—O—C or Si—O—Glass interactions, confirming the embedded glass fiber reinforcement in the composite structure. The characteristic epoxide ring vibrations were identified in the range of 933–939 cm^{-1}, which are indicative of unreacted or partially reacted epoxide groups within the resin. The presence of N—H bending vibrations from the amine curing agent was observed at 551–559 cm^{-1}, further validating the expected chemical network formation. These spectral assignments are in agreement with previous literature. For instance, Mamalis et al. [34] documented O—H and epoxide bands in the 3200–3600 cm^{-1} and 933–939 cm^{-1} regions, respectively, while Fernandesa et al. [35] also confirmed Si—O and Si—Glass bands between 971 and 1093 cm^{-1}.

The summary of key FTIR peak positions for all specimens across the curing temperatures is provided in Table 1, supporting the consistency of the chemical structure and the successful integration of all three composite phases (epoxy, silica, and glass fiber).

5.3 | XRD Analysis

XRD analysis was conducted to investigate the crystallinity and phase composition of the epoxy–silica composite samples cured at different temperatures. The XRD patterns corresponding to curing temperatures of 60°C, 80°C, 100°C, 120°C, 140°C, and 160°C are shown in Figure 3a–f. The diffraction patterns for all samples exhibited a characteristic broad diffuse hump between 10° and 20° (2θ), indicative of a predominantly amorphous structure. This broad halo is typical for polymeric materials such as epoxy resins, where the lack of long-range order results in the absence of sharp Bragg diffraction peaks. The observation of such an amorphous profile across all curing temperatures suggests that the crosslinked epoxy matrix maintained its non-crystalline character, even after filler addition and thermal curing. Notably,

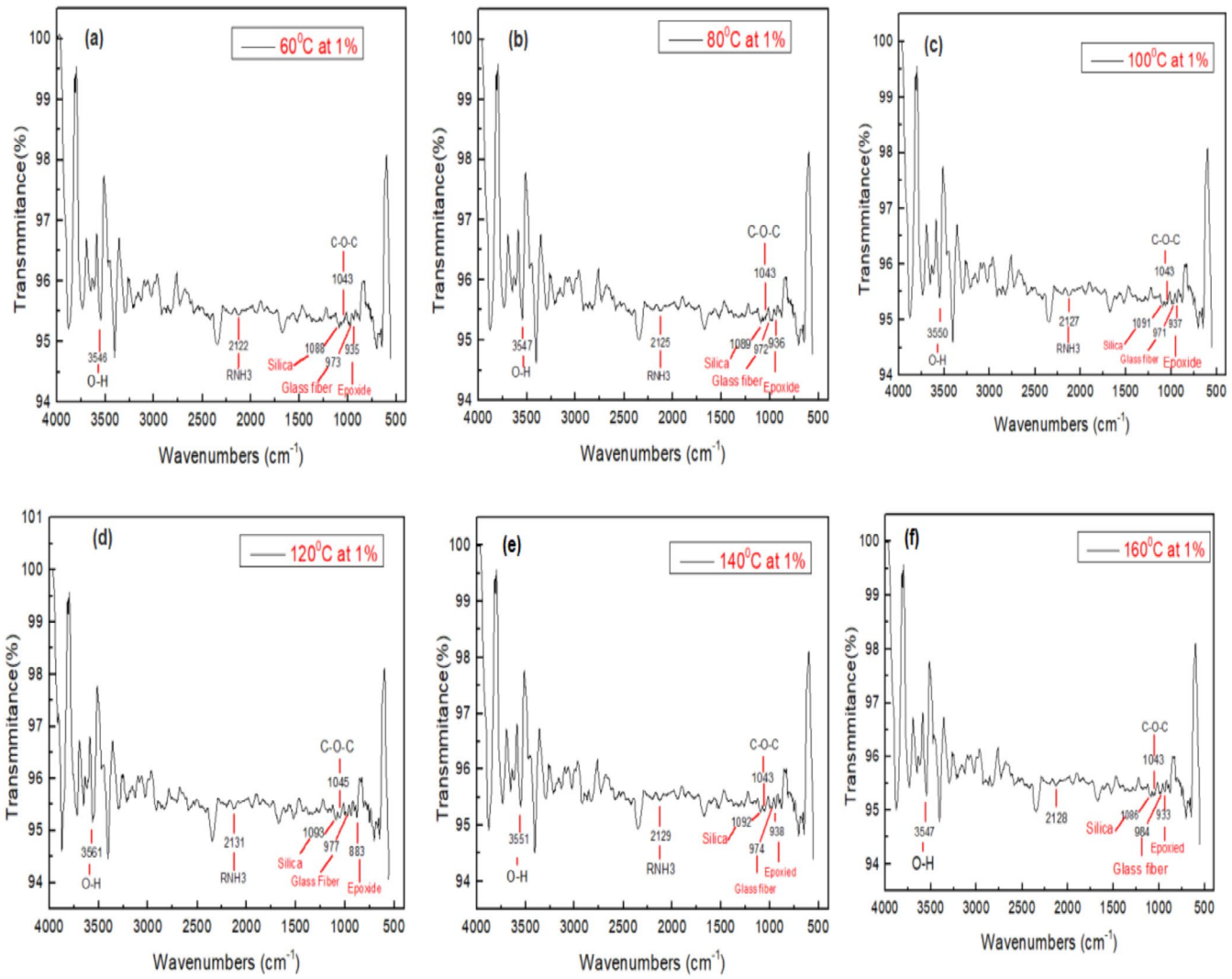

FIGURE 2 | FTIR analysis of samples at curing temperatures of (a) 60°C (b) 80°C (c) 100°C (d) 120°C (e) 140°C and (f) 160°C.

TABLE 1 | Specimen peaks at various curing temperatures in wavenumber (cm^{-1}).

Temperature	OH	RNH3	Silica	C—O—C	Glass fiber	Epoxide
60°C	3546	2122	1088	1043	973	935
80°C	3547	2125	1089	1043	972	936
100°C	3550	2127	1091	1043	971	937
120°C	3561	2131	1093	1045	977	939
140°C	3551	2129	1092	1043	974	938
160°C	3547	2128	1086	1043	984	933

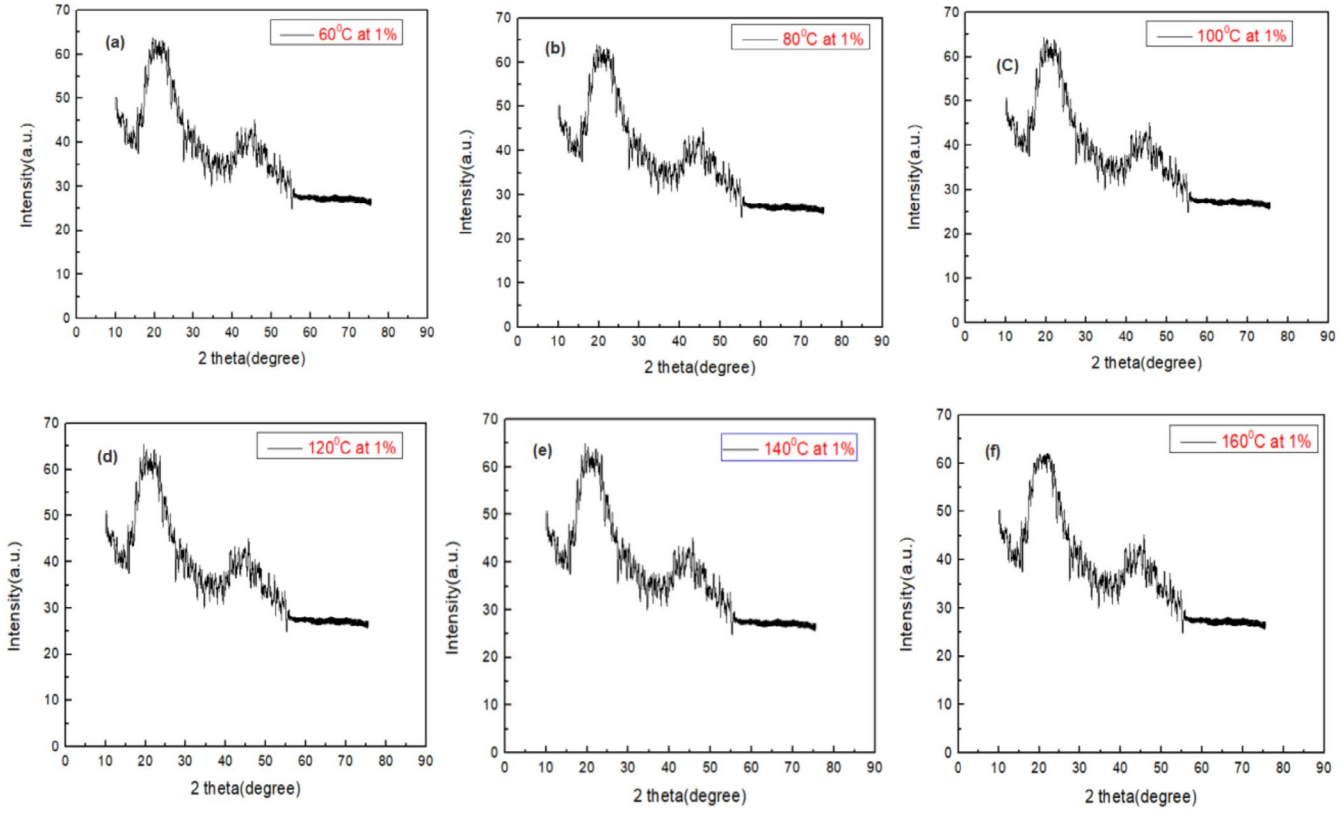

FIGURE 3 | XRD spectra of samples cured at (a) 60°C (b) 80°C (c) 100°C (d) 120°C (e) 140°C, and (f) 160°C.

no significant crystalline peaks attributable to the silica microparticles or glass fibers were observed within the scanned range. This can be attributed to several factors: the relatively low concentration and fine dispersion of silica fillers within the matrix, the inherently amorphous nature of the epoxy, and the possible overlap or masking of weak crystalline signals by the dominant amorphous background. Furthermore, the XRD spectra for neat epoxy, silica powder, and glass fiber-reinforced composites at various curing temperatures showed no substantial differences, reinforcing the conclusion that the composite's microstructure remained largely amorphous irrespective of curing temperature. These results are consistent with prior studies which also reported the predominance of amorphous features in silica-filled epoxy composites [36–38]. XRD patterns for all curing temperatures display a broad halo centered near $2\theta = 22°–25°$, characteristic of the amorphous epoxy matrix and E-glass fibers. The absence of sharp crystalline peaks from SiO_2 is expected because the silica used is amorphous (fumed silica), which exhibits only diffuse scattering. Moreover, the strong amorphous background of the epoxy matrix masks any low-intensity short-range ordering from the silica network. Similar patterns have been reported for silica-epoxy and E-glass/epoxy systems, where only a single amorphous halo is observed even at silica contents up to 15–20 wt%. This confirms that the composite microstructure remains amorphous after curing, with no undesired crystallization induced by thermal treatment up to 160°C. The XRD analysis confirms that the incorporation of silica particles and glass fibers did not induce any significant crystallization or phase separation within the composite, which is desirable for maintaining uniform mechanical and thermal behavior throughout the material.

5.4 | TGA

TGA was performed on all composite specimens cured at different temperatures to assess their thermal degradation behavior and stability. The TGA profiles for the samples are depicted in Figure 4. The thermal degradation of the composites occurred in two distinct stages: First degradation stage (50°C–350°C) which corresponds primarily to the decomposition of low-molecular-weight species, residual unreacted monomers, absorbed moisture, and the initial breakdown of organic matrix chains. The percentage of weight loss during this stage varied across different curing temperatures, indicating the influence of curing conditions on the degree of polymerization and thermal resistance (Table 2). Second degradation stage (350°C–600°C) which is associated with the degradation of the crosslinked epoxy network and the further breakdown of the composite's structural framework. The onset of significant mass loss at higher temperatures reflects the composite's ability to resist thermal degradation until elevated thermal stresses are imposed. Among all the specimens, the composite cured at 120°C exhibited the highest thermal stability, with the greatest residual mass after both degradation stages. This suggests that 120°C represents an optimum curing temperature for achieving maximum crosslink density and enhanced thermal durability in the epoxy–silica composite system. Additionally, theoretical calculations of degradation kinetics showed close agreement with the experimental TGA results, thereby validating the assumed degradation models [39, 40]. The 160°C specimen exhibits a low char yield (1.14%), consistent with extensive volatilization of organic matrix; however, char yield alone is not a direct indicator of stability in thermoset epoxies. Based on $T_{5\%}$, T_{max}, and E_a (KAS),

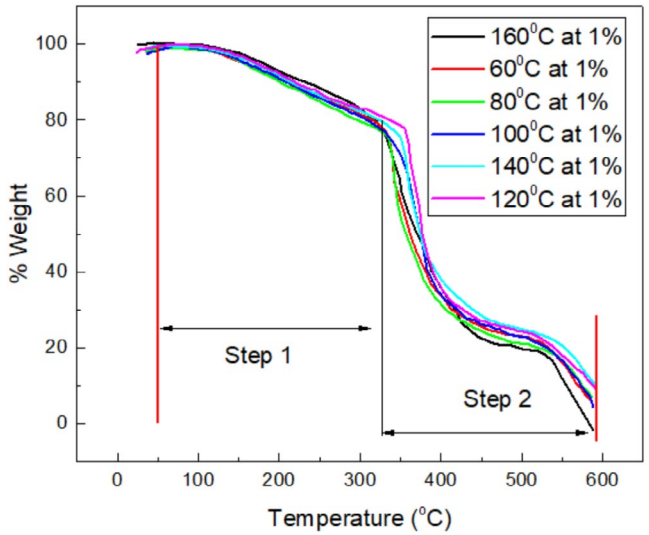

FIGURE 4 | Specimen weight loss at various curing temperatures (60°C–160°C) by TGA analysis.

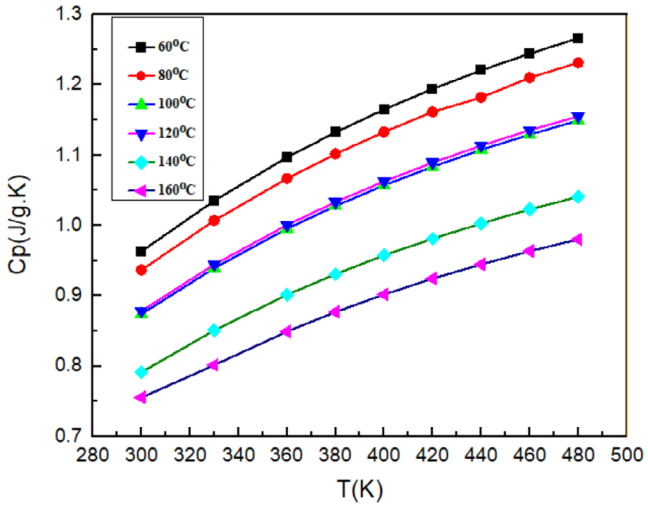

FIGURE 5 | C_p experimental and theoretical computations with changing curing temperature (60°C–160°C).

TABLE 2 | Specimen peaks at various curing temperature.

Specimen curing temperature (°C)	% weight of specimen remaining at initial degradation stage (50°C–350°C)	% weight of specimen remaining at second degradation stage (350°C–600°C)
60°C	58.40	5.22
80°C	53.19	6.28
100°C	71.11	6.40
120°C	75.81	10.17
140°C	75.90	10.80
160°C	79.09	1.14

the 120°C–140°C cures display the most favorable thermal resistance, while 120°C offers the best thermal–mechanical balance observed in this study. It was observed that the composites cured at higher temperatures generally exhibited higher activation energies, implying that greater thermal energy input is required to initiate degradation for better-cured samples, further confirming their superior thermal resistance (Refer to Table 2).

5.5 | Specific Heat Capacity

The specific heat capacity (C_p) of the epoxy–silica composite specimens was determined experimentally in accordance with ASTM E-1269 using DSC. The C_p values were plotted as a function of specimen temperature to evaluate the thermal energy absorption characteristics of composites cured at different temperatures, as shown in Figure 5. The analysis revealed a clear trend that C_p values decreased with increasing curing temperature. This behavior indicates that composites cured at higher temperatures possess lower heat retention capacity compared to those cured at lower temperatures. From a physical perspective, the enhanced crosslink density achieved at elevated curing temperatures reduces the segmental mobility of polymer chains, leading to decreased ability to store thermal energy within the matrix structure. This reduction in C_p implies that composites prepared at higher curing temperatures will absorb and retain less heat, which is particularly advantageous for applications involving pressure vessels and pipelines. Lower heat retention correlates with reduced internal heat buildup, minimized thermal expansion, and better thermal shock resistance, thereby improving operational safety and stability under fluctuating thermal environments. Among all samples, the specimen cured at 120°C demonstrated an optimal balance of mechanical and thermal properties, including favorable specific heat capacity characteristics. Therefore, 120°C is identified as the optimum curing temperature for manufacturing thin-walled vessels and pipes using this three-phase composite system. Furthermore, the theoretical predictions of C_p based on numerical models showed strong agreement with the experimental data, validating the reliability of the underlying thermophysical assumptions and experimental methodologies employed in this study.

Curve fitting of Equation (19) was performed on the experimental C_p values. The curve fitting based on Equation (19) on experimentally available data is validated by ANNOVA analysis which validates that theoretical estimations were 95% significant, that is, $p < 0.05$ for all the curing temperatures. This further implies that derived Relation (19) can fully estimate the C_p with high significance, that is, more than 95% accuracy (Table 3). Moreover, C_p estimated for all the curing temperatures, that is, 60°C to 160°C are accurately predicted by Equation (19). Besides, the individual parametric analysis was also performed based on type-III partial ANNOVA for each term of the Equation (19), that is, p values for linear, quadratic and combination block (linear and quadratic) are all less than 0.05 accordingly (as clearly evident in Table 4) which eventually means the estimated values of C_p are determined with higher confidence.

5.6 | Thermal Conductivity

The thermal conductivity (λ) of the epoxy–silica composite specimens was experimentally measured in accordance with ASTM E-1530 using a guarded heat flow meter. λ of polymer-based composites is dominated by phonon (lattice vibration) transport, since electron conduction is negligible. Using the mathematical concept of kinetic theory:

$$\lambda = \frac{1}{3} C_v v_{\text{phonon}} l \tag{37}$$

where C_v is the volumetric heat capacity, v_{phonon} is the average phonon group velocity, and l is the phonon mean free path (MFP). Atomic-scale disorder in the form of randomly crosslinked epoxy chains, silica particle–matrix interface mismatch, and voids strongly reduces l by introducing elastic scattering sites. Each scattering event interrupts phonon propagation, lowering net energy transport. In contrast, crosslink density enhanced when curing was performed on 120°C generates topological disorder (random orientation and misfit at interfaces), maximizing phonon scattering and leading to the observed relatively lower λ. Beyond 120°C, network densification and stress relaxation slightly improve interfacial continuity, effectively increasing l and partially restoring λ. This explains why λ decreases initially with disorder, then further reduces λ probably due to more ordered and tightly cross-linked. Moreover, at 160°C the heat transport shifts towards diffusion rather than phonon

TABLE 3 | ANOVA analysis for curve fitting of Equation (19) on experimental data for estimating C_p.

Curing temperature (°C)	Regression	DOF	Sum of squares	Mean square	*F* value	*p*
60	Model	2	0.05521	0.0276	4637.5	<0.05
	Error	7	4.17×10^{-5}	5.95×10^{-6}		
	Total	9	0.05525			
80	Model	2	0.05057	0.02529	2590.256	<0.05
	Error	7	6.83×10^{-5}	9.76×10^{-6}		
	Total	9	0.05064			
100	Model	2	0.0449	0.02245	2736.806	<0.05
	Error	7	5.74×10^{-5}	8.20×10^{-6}		
	Total	9	0.04496			
120	Model	2	0.04044	0.02022	2956.37	<0.05
	Error	7	4.79×10^{-5}	6.84×10^{-6}		
	Total	9	0.04049			
140	Model	2	0.04301	0.02151	1991.247	<0.05
	Error	7	7.56×10^{-5}	1.08×10^{-6}		
	Total	9	0.04309			
160	Model	2	0.0394	0.0197	3514.122	<0.05
	Error	7	3.92×10^{-5}	5.61×10^{-6}		
	Total	9	0.03944			

TABLE 4 | Type-III partial F ANOVA analysis for Equation (19) on experimental data to find the significance of individual parameters, that is, interaction in combination or block (linear + quadratic), intercept, respective slopes of linear and quadratic or 2nd order term.

T_{Cur}	DOF_E	MS_E	SS_E	R^2	F_{linear}	p_{linear}	F_{Quad}	P_{quad}	$F_{\text{block(lin+quad)}}$	p_{block}
60°C	7	5.95×10^{-6}	4.16×10^{-6}	0.9992	9195.4545	<0.05	79.545	<0.05	4637.5	<0.05
80°C	7	9.76×10^{-6}	6.83×10^{-5}	0.9986	5167.3968	<0.05	13.115	<0.05	2590.256098	<0.05
100°C	7	1.74×10^{-6}	0.00012	0.9973	2595.0074	<0.05	17.326	<0.05	1306.167079	<0.05
120°C	7	5.22×10^{-6}	0.00036	0.9913	786.36914	<0.05	19.873	<0.05	403.121319	<0.05
140°C	7	1.08×10^{-5}	7.56×10^{-6}	0.9982	3945.3907	<0.05	37.104	<0.05	1991.247495	<0.05
160°C	7	5.60×10^{-6}	3.92×10^{-5}	0.9990	7005.4054	<0.05	22.837	<0.05	3514.121622	<0.05

propagation and as a consequence, minimum value of λ was recorded [41]. Lower λ value of 160°C cured specimen are possibly due to combinatory effect of SiO_2 agglomeration accompanied with premature curing. The results, presented in Figure 6, were also compared with theoretical predictions derived from the thermal conductivity model suggested in this research. The experimental data reveal a general trend of increasing thermal conductivity with increasing curing temperature. This behavior can be attributed to the stabilization of the polymer network at higher curing temperatures, which results in enhanced continuity of the molecular chains and more efficient phonon transport. As crosslinking becomes more complete, the number of scattering centers (voids, unreacted groups, chain ends) decreases, thus facilitating thermal conduction through the matrix. Interestingly, while thermal conductivity rises with externally supplied temperature overall, the composite cured at 120°C exhibited the relatively lower λ value based on balanced or overall comparison/s. This suggests that at 120°C, a balanced crosslinking density is achieved sufficiently to ensure structural integrity while still maintaining a degree of atomistic disorder and interface scattering that effectively reduces heat transfer. This reduced thermal conductivity is particularly desirable for thin-walled pressure vessels and pipe applications, where thermal insulation is critical to minimize heat loss, prevent thermal fatigue, and maintain internal fluid temperatures. The observed trend is consistent with the concept that beyond a certain curing threshold, increased polymer ordering may also hinder heat flow possibly due to premature resin absorbing heat to possibly fully cure eventually reducing heat transfer. Furthermore, the theoretical λ values obtained using second-order polynomial models, that is, Equation (22) showed a strong correlation with experimental results, confirming the accuracy and predictive capability of the thermal model derived and curve fitted. Based on the overall findings, 120°C is once again validated as the optimum curing temperature not only for mechanical performance but also for achieving competitive thermal conductivity, making the composite highly suitable for demanding thermal environments.

In the case of λ, curve fitting of Equation (22) was performed on the experimental λ values. The curve fitting based on Equation (22) on experimentally available data is validated by the outcome of ANNOVA analysis which implies that theoretical approximations were highly significant, that is, $p<0.05$ or 95% credible (after applying to all the curing temperatures, that is, 60°C–160°C) as overall relationship (Table 5). This further depicts that Equation (22) can overall predict λ for all the samples prepared at various curing temperatures with higher significance level or confidence interval, that is, more than 95% accurately (As evidenced in Figure 6 and Table 5). Furthermore, the individual parametric analysis was also performed based on type-III partial p-test for each term of the Equation (22), that is, p values for linear, quadratic and combination block (linear and quadratic) are all less than 0.05 accordingly (Table 6). Hence, the interaction is highly desirable between input and out parameter/s.

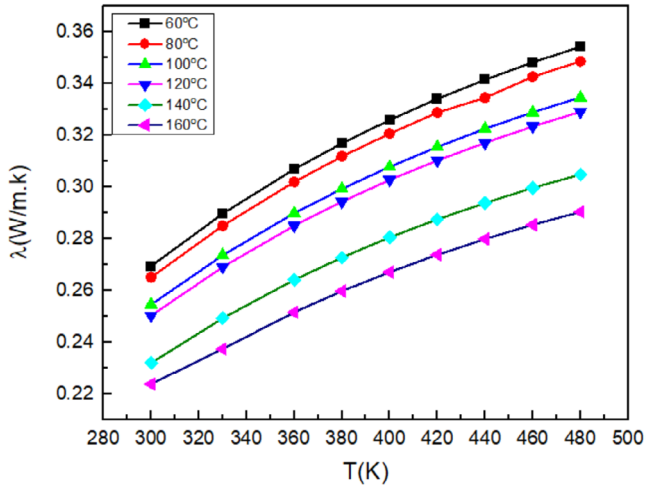

FIGURE 6 | Experimental and theoretical calculations of thermal conductivity at various curing temperatures.

5.7 | Hoop Strength

The hoop strength (S_H) of the fabricated composite specimens was evaluated both experimentally and theoretically across a range of curing temperatures from 60°C to 160°C. The experimental determination was carried out in accordance with ASTM D2290 [42], which provides standardized methodology for split-disk testing of filament-wound composite rings. The measured hoop strength values for specimens cured at 60°C, 80°C, 100°C, 120°C, 140°C, and 160°C were found to be 296.7 ± 5.2 MPa, 315.6 ± 5.7 MPa, 326.0 ± 6.2 MPa, 341.3 ± 6.5 MPa, 343.8 ± 6.9 MPa, and 260.1 ± 4.2 MPa, respectively, as shown in Figure 7. A clear trend of increasing hoop strength with increasing curing temperature was observed from 60°C to 140°C. This improvement is attributed to enhanced molecular crosslinking and polymer chain alignment, which together improve the structural integrity and load-bearing capacity of the matrix. Additionally, controlled thermal curing promotes interfacial adhesion between the epoxy matrix, silica filler, and glass fibers, further contributing to the material's resistance to circumferential stresses. However, at 160°C, a noticeable decrease in hoop strength was observed. This decline is likely due to thermal over-curing, which can result in microstructural degradation, such as resin embrittlement, residual stress buildup, and the formation of micro-voids or cracks. Excessive heat may also break down the chemical bonds within the polymer network, ultimately reducing the mechanical performance of the composite. Based on both experimental measurements and the corresponding theoretical predictions, the composite cured at 120°C demonstrated the most favorable hoop strength, striking a balance between crosslink density and material toughness. The decrease in mechanical properties at 160°C is attributed to over-curing, which induces excessive crosslinking and reduces the free volume of the epoxy matrix. This phenomenon leads to matrix brittleness and early crack initiation. Similar behavior has been reported for epoxy composites cured at elevated temperatures [43]. This finding reinforces the conclusion that 120°C is the optimal curing temperature for maximizing mechanical strength in thin-walled composite vessels subjected to internal pressure.

The outcome, that is, S_H is fully supported by the type-III partial p ANNOVA analysis which validates that each interaction and parameters is significant in this analysis, that is, p_{linear}, p_{quad}, p_{cubic}, and p_{block} are less than 0.05 accordingly (Table 7).

TABLE 5 | ANOVA analysis for curve fitting of Equation (22) on experimental data for approximating λ.

Curing temperature (°C)	Regression	DOF	Sum of squares	Mean square	*F* value	*p*
60°C	Model	2	0.00301	0.00151	456.3503	<0.05
	Error	7	2.31×10^{-5}	3.30×10^{-6}		
	Total	9	0.00304			
80°C	Model	2	0.00302	0.00151	843.4535	<0.05
	Error	7	1.25×10^{-5}	1.79×10^{-6}		
	Total	9	0.00303			
100°C	Model	2	0.00339	0.0017	448.0516	<0.05
	Error	7	2.65×10^{-5}	3.79×10^{-6}		
	Total	9	0.00342			
120°C	Model	2	0.00378	0.00189	525.0532	<0.05
	Error	7	2.52×10^{-5}	3.60×10^{-6}		
	Total	9	0.00381			
140°C	Model	2	0.00386	0.00193	671.1763	<0.05
	Error	7	2.02×10^{-5}	2.88×10^{-6}		
	Total	9	0.00388			
160°C	Model	2	0.00417	0.00208	745.2124	<0.05
	Error	7	1.96×10^{-5}	2.80×10^{-6}		
	Total	9	0.00419			

TABLE 6 | Type-III partial F-ANNOVA analysis for Equation (22) on experimental data to find the significance of individual parameters, that is, interaction in combination or block (linear + quadratic), intercept, respective slopes of linear and quadratic or 2nd order term validation.

T_{Cur}	DOF_E	MS_E	SS_E	R^2	F_{linear}	p_{linear}	F_{quad}	P_{quad}	$F_{block(lin+quad)}$	p_{block}
60°C	7	3.30×10^{-6}	2.31×10^{-5}	0.9924	856.1625	<0.05	56.5381	<0.05	456.3503	<0.05
80°C	7	1.79×10^{-6}	1.25×10^{-5}	0.9959	1589.151	<0.05	97.7563	<0.05	843.4535	<0.05
100°C	7	3.79×10^{-6}	2.65×10^{-5}	0.9922	831.2588	<0.05	64.8445	<0.05	448.0516	<0.05
120°C	7	3.60×10^{-6}	2.52×10^{-5}	0.9934	968.4916	<0.05	81.6148	<0.05	525.0532	<0.05
140°C	7	2.88×10^{-6}	2.01×10^{-5}	0.9948	1239.184	<0.05	103.1684	<0.05	671.1763	<0.05
160°C	7	2.79×10^{-6}	1.95×10^{-5}	0.9953	1370.996	<0.05	119.429	<0.05	745.2124	<0.05

5.8 | Burst Pressure

Burst pressure in Equation (37) [44] was measured theoretically by the following relationship:

$$S_H = \frac{P_b(d+t)}{2t} \tag{38}$$

where S_H, P_b, d, and t are hoop strength, burst pressure, thickness and inner diameter of pipe/tube, respectively. The computed P_b values for specimens cured at 60°C, 80°C, 100°C, 120°C, 140°C, and 160°C were 15.21 ± 0.27 MPa, 16.19 ± 0.29 MPa, 16.71 ± 0.32 MPa, 17.50 ± 0.33 MPa, 17.63 ± 0.35 MPa, and 13.34 ± 0.20 MPa, respectively, as illustrated in Figure 8.

An increasing trend in burst pressure was observed as the curing temperature was raised from 60°C to 140°C. This enhancement is primarily attributed to improved crosslinking density, matrix consolidation, and enhanced fiber-matrix interfacial bonding achieved through elevated thermal activation. The increased matrix rigidity and adhesion contribute to the composite's ability to resist hoop stresses and internal pressure loads without failure. The specimen cured at 120°C demonstrated optimal burst pressure performance, closely followed by the one cured at 140°C. However, a decline in burst pressure was observed for the specimen cured at 160°C, which is consistent with previously observed reductions in hoop strength. This degradation is likely due to thermal over-curing, which can cause excessive crosslinking, resin embrittlement, or the development

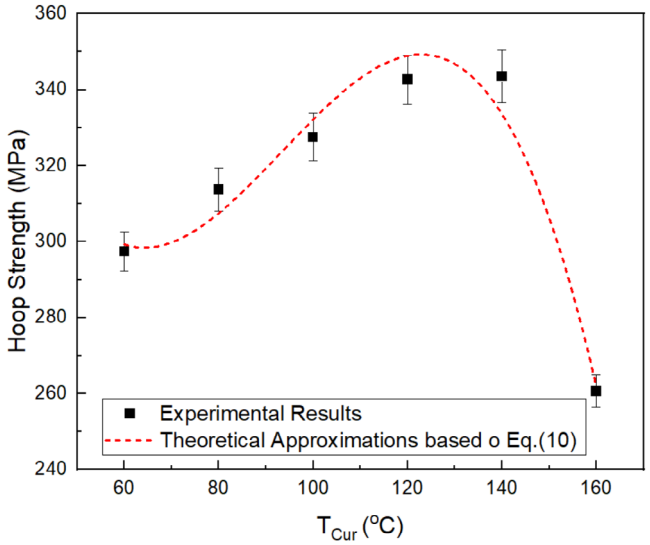

FIGURE 7 | Experimental and theoretically calculated hoop strength at various curing temperatures.

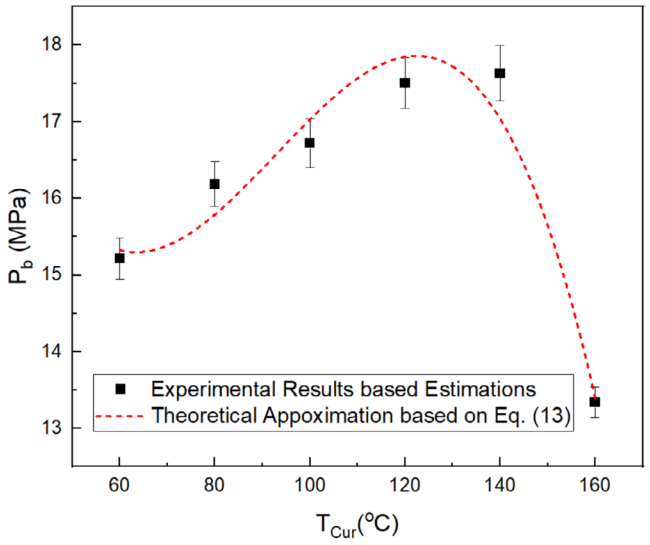

FIGURE 8 | Experimental and theoretically determined burst pressure with increasing curing temperature.

TABLE 7 | Type-III ANOVA partial *p* analysis based on 3 replications per curing temperature and considering $\alpha = 0.05$ to investigate the significance of each parameter.

Description	Corresponding value
N	18.00
DOF	14.00
SS_E	1000.34
MS_E	71.45
R^2	0.94
F_{linear}	33.16
p_{linear}	< 0.05
$F_{quadratic}$	149.87
$p_{quadratic}$	< 0.05
F_{cubic}	47.73
p_{cubic}	< 0.05
F_{block}(lin+quad+cubic)	67.15
p_{block}	< 0.05

TABLE 8 | Type-III ANOVA partial *p* analysis based on three replications per curing temperature and considering $\alpha = 0.05$ to investigate the significance of each parameter.

Description	Corresponding value
N	18
DOF	14
SS_E	3.218637
MS_E	0.229903
R^2	0.920333
F_{linear}	25.42809
p_{linear}	< 0.05
$F_{quadratic}$	121.1671
$p_{quadratic}$	< 0.05
F_{cubic}	37.17845
p_{cubic}	< 0.05
$F_{block(lin+quad+cubic)}$	53.91034
p_{block}	< 0.05

of microscopic defects such as voids and microcracks [11]. These defects weaken the overall structural integrity of the composite, making it more susceptible to pressure-induced failure. Therefore, both the trend of increasing burst pressure with curing temperature and its subsequent decline at excessive heat exposure reinforce the conclusion that 120°C represents the optimal curing condition for maximizing pressure-handling capacity in the fabricated epoxy–silica–glass fiber composite pipes. Analysis of variance (ANOVA) reveals that results predicted by third degree polynomial estimated results with more than 95% confidence and accuracy (as shown in Table 8). In other words, the *p* value is 1.26×10^{-8} which is much lower than 0.05. This ultimately shows that interaction is highly significant, that is, the difference in values of pipes fabricated at each curing temperature is substantially different.

The outcome is fully supported by the type-III partial *p* ANNOVA analysis which validates that each interaction and parameters (T_{cur} and P_b) is significant in this analysis, that is, p_{linear}, p_{quad}, p_{cubic}, and p_{block} are less than 0.05 accordingly (Table 8).

5.9 | Factor of Safety

The FOS for the composite vessels was theoretically estimated by taking the ratio of the experimentally determined hoop

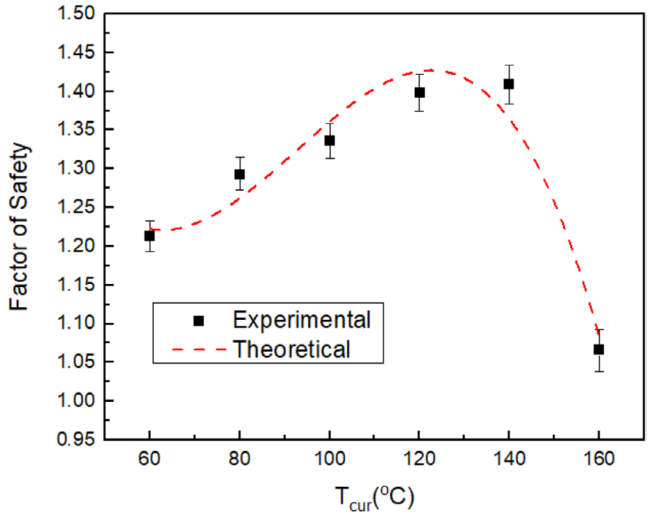

FIGURE 9 | *FOS* based on experimental and theoretical calculations.

strength (S_H) to the von Mises equivalent stress (σ_{VM}.), as described previously. The FOS values for the specimens cured at 60°C, 80°C, 100°C, 120°C, 140°C, and 160°C were calculated as 1.21 ± 0.02, 1.29 ± 0.021, 1.34 ± 0.023, 1.39 ± 0.024, 1.40 ± 0.025, and 1.06 ± 0.027, respectively, as presented in Figure 9.

A progressive increase in *FOS* was observed as the curing temperature was elevated from 60°C to 120°C. This trend correlates with the simultaneous improvements in hoop strength, burst pressure, and material crosslinking observed across the same temperature range. The maximum FOS was achieved at 120°C, indicating that composites cured at this temperature offer the highest margin of safety against mechanical failure under internal pressure loading. Beyond the optimal curing temperature, at 160°C, a significant drop in FOS was recorded. This reduction is attributed to premature degradation of the polymer network, likely caused by over-curing effects, microvoid formation, and loss of structural cohesion. Such thermal overexposure compromises the mechanical properties and, consequently, reduces the material's ability to sustain loads safely. Thus, based on the FOS analysis, it can be concluded that 120°C represents the optimal curing temperature, providing the highest safety factor and ensuring reliable and robust performance for thin-walled vessel applications under pressure.

6 | Conclusions

Based on the comprehensive experimental and theoretical analysis involving material characterization, pipe fabrication, and mechanical and thermal performance evaluation, the following key conclusions can be drawn:

1. FTIR spectroscopy confirmed the successful chemical integration of SiO_2 micro-particles and glass fiber reinforcements within the epoxy matrix, forming a robust three-phase composite structure. Similarly, XRD analysis exhibited a predominantly amorphous pattern across all samples, with no significant crystalline peaks detected, further validating the effective fabrication and homogeneous distribution of constituents within the composite system.
2. The S_H exhibited significant improvements of 6.37%, 10.0%, 15.0%, and 15.1% at curing temperatures of 80°C, 100°C, 120°C, and 140°C, respectively, relative to the baseline 60°C specimen. This trend is attributed to enhanced molecular disorder and controlled defect formation within the polymer matrix, consistent with a third-degree polynomial relationship. Similarly, P_b demonstrated a corresponding increase of 6.35%, 10.00%, 15.05%, and 15.5% with rising curing temperatures up to 140°C, reflecting improved matrix consolidation and fiber-matrix adhesion. Both S_H and P_b trends are strongly correlated with the thermal curing behavior, affirming the critical role of curing temperature in mechanical performance optimization.
3. λ decreased steadily with curing temperature, dropping by 1.5%–17% at 300 K for cures between 80°C and 160°C. This decline reflects increased phonon scattering from atomic-scale disorder and limited crosslink densification near the optimal cure. Second-order polynomial regression of Equation (22) provided an excellent fit to the DTC experimental data confirming the predictive reliability of the derived model. C_p exhibited a similar downward trend, decreasing by 3%–22% over the same temperature range. The concurrent reduction in λ and C_p indicates improved thermal insulation and reduced heat capacity. This concurrent reduction in C_p and λ highlights the improved thermal insulation characteristics of the composites.
4. The calculated FOS for all specimens was significantly higher than the corresponding σ_{VM}., demonstrating that the fabricated vessels can reliably withstand internal pressures around 100 MPa without risk of structural failure. These findings further suggest that the developed epoxy/SiO_2/glass fiber composites offer a viable and advantageous alternative to traditional metallic vessels, owing to their higher strength-to-weight ratios and enhanced thermal stability.

Acknowledgments

This article has been produced with the financial support of the European Union under the REFRESH—Research Excellence For REgion Sustainability and High-tech Industries project number CZ.10.03.01/00/22_003/0000048 via the Operational Programme Just Transition. We also acknowledge the support of Polymer Industries, Gujranwala and Kinetix Automation Controls (pvt) Ltd for providing support as per requirement.

Conflicts of Interest

The authors declare no conflicts of interest.

Data Availability Statement

The data that support the findings of this study are available from the corresponding author upon reasonable request.

References

1. Z. Rubab, A. Afzal, H. M. Siddiqi, and S. Saeed, "Preparation, Characterization, and Enhanced Thermal and Mechanical Properties of Epoxy-Titania Composites," *Scientific World Journal* 2014 (2014): 1–7, https://doi.org/10.1155/2014/515739.

2. V. Vijayarajan and R. Murugananandhan, "Impact Analysis of Carbon/Glass/Epoxy Hybrid Composite Pipes," *International Journal of Recent*

Technology and Engineering 8 (2019): 6002–6006, https://doi.org/10.35940/ijrte.c4798.118419.

3. F. U. Buehler and J. C. Seferis, "Effect of Reinforcement and Solvent Content on Moisture Absorption in Epoxy Composite Materials," *Composites Part A: Applied Science and Manufacturing* 31 (2000): 741–748, https://doi.org/10.1016/S1359-835X(00)00036-1.

4. M. M. Davoodi, S. M. Sapuan, D. Ahmad, A. Ali, A. Khalina, and M. Jonoobi, "Mechanical Properties of Hybrid Kenaf/Glass Reinforced Epoxy Composite for Passenger Car Bumper Beam," *Materials and Design* 31 (2010): 4927–4932, https://doi.org/10.1016/j.matdes.2010.05.021.

5. H. Singh, G. Singh Brar, H. Kumar, and V. Aggarwal, "A Review on Metal Matrix Composite for Automobile Applications," *Materials Today: Proceedings* 43 (2020): 320–325, https://doi.org/10.1016/j.matpr.2020.11.670.

6. M. Manoj Prabhakar, N. Rajini, N. Ayrilmis, et al., "An Overview of Burst, Buckling, Durability and Corrosion Analysis of Lightweight FRP Composite Pipes and Their Applicability," *Composite Structures* 230 (2019): 111419, https://doi.org/10.1016/j.compstruct.2019.111419.

7. A. Kausar, I. Rafique, and B. Muhammad, "Review of Applications of Polymer / Carbon Nanotubes and Epoxy / CNT Composites," *Polymer-Plastics Technology and Engineering* 55 (2016): 2559, https://doi.org/10.1080/03602559.2016.1163588.

8. Ç. Uzay, "Investigation of Physical, Mechanical, and Thermal Properties of Glass Fiber Reinforced Polymer Composites Strengthened With KH550 and KH570 Silane-Coated Silicon Dioxide Nanoparticles," *Journal of Composite Materials* 56 (2022): 2995–3011, https://doi.org/10.1177/00219983221108531.

9. Y. Wen, C. Chen, Y. Ye, et al., "Advances on Thermally Conductive Epoxy-Based Composites as Electronic Packaging Underfill Materials—A Review," *Advanced Materials* 34 (2022): 2201023, https://doi.org/10.1002/adma.202201023.

10. T. Zheng, H. Xi, Z. Wang, et al., "The Curing Kinetics and Mechanical Properties of Epoxy Resin Composites Reinforced by PEEK Microparticles," *Polymer Testing* 91 (2020): 106781, https://doi.org/10.1016/j.polymertesting.2020.106781.

11. A. Hawa, M. S. Abdul Majid, M. Afendi, et al., "Burst Strength and Impact Behaviour of Hydrothermally Aged Glass Fibre/Epoxy Composite Pipes," *Materials & Design* 89 (2016): 455–464, https://doi.org/10.1016/j.matdes.2015.09.082.

12. M. Tănase, A. Diniță, G. Lvov, and A. I. Portoacă, "Experimental Determination of Circumferential Mechanical Properties of GFRP Pipes Using the Split-Disk Method: Evaluating the Impact of Aggressive Environments," *Applied Sciences* 14 (2024): 11845, https://doi.org/10.3390/app142411845.

13. B. Kusuma, C. S. Saran, and A. Satapathy, "Thermal Conductivity of Glass Dust Filled Epoxy Composite: A Numerical and Experimental Study," *Polymer Composites* 46 (2025): 14476–14490, https://doi.org/10.1002/pc.30075.

14. J. You, Y. Zhao, and B. Zhang, "Numerical and Experimental Study on Balanced Performance and Axial Stiffness of Fiber-Reinforced Rubber Pipe," *Polymers* 16 (2024): 2088, https://doi.org/10.3390/polym16142088.

15. Y. Akın and M. Kara, "Mechanical Strength and Low-Velocity Impact Behavior of Glass Fiber Reinforced Filament Wound Pipes With Different Number of Layers After Hydrothermal Aging," *Journal of Composite Materials* 58 (2024): 2111–2129, https://doi.org/10.1177/00219983241260881.

16. F. C. Shen, "A Filament-Wound Structure Technology Overview," *Materials Chemistry and Physics* 42 (1995): 96–100, https://doi.org/10.1016/0254-0584(95)01554-X.

17. R. Wazalwar, M. Sahu, and A. M. Raichur, "Mechanical Properties of Aerospace Epoxy Composites Reinforced With 2D Nano-Fillers: Current Status and Road to Industrialization," *Nanoscale Advances* 3 (2021): 2741–2776, https://doi.org/10.1039/d1na00050k.

18. N. Maqsood, A. Khan, M. K. Alamgir, S. A. Shah, and M. Fahad, "PTFE Thin Film Coating on 316L Stainless Steel for Corrosion Protection in Acidic Environment," *Journal of Engineering and Applied Science* 36 (2017): 183–190.

19. X. Wang, X. Qi, Z. Lin, and D. Battocchi, "Graphene Reinforced Composites as Protective Coatings for Oil and Gas Pipelines," *Nanomaterials* 8 (2018): 8, https://doi.org/10.3390/nano8121005.

20. Y. Cao, Z. Li, L. Gan, N. Wang, and Y. Bai, "Mechanical Properties Study of Fiberglass Reinforced Flexible Pipeline in Marine Applications," *Ships and Offshore Structures* 20, no. 10 (2024): 1458–1474, https://doi.org/10.1080/17445302.2024.2397286.

21. D. Kuanhai, L. Jialian, L. Bin, P. Lin, L. Wanying, and L. Yuanhua, "Study of Internal Pressure Strength of the Titanium-Steel Composite Tube Based on Yield and Shear Failure Mechanisms," *International Journal of Hydrogen Energy* 44 (2019): 2997–3012, https://doi.org/10.1016/j.ijhydene.2018.11.201.

22. L. Smith, "Control of Corrosion in Oil and Gas Production Tubing," *British Corrosion Journal* 34 (1999): 247–253, https://doi.org/10.1179/000705999101500905.

23. R. Emberley, C. G. Putynska, A. Bolanos, et al., "Description of Small and Large-Scale Cross Laminated Timber Fire Tests," *Fire Safety Journal* 91 (2017): 327–335, https://doi.org/10.1016/j.firesaf.2017.03.024.

24. D. Sánchez-Rodríguez, H. Eloussifi, J. Farjas, P. Roura, and M. Dammak, "Thermal Gradients in Thermal Analysis Experiments: Criterions to Prevent Inaccuracies When Determining Sample Temperature and Kinetic Parameters," *Thermochimica Acta* 589 (2014): 37–46, https://doi.org/10.1016/j.tca.2014.05.001.

25. S. Vyazovkin, A. K. Burnham, J. M. Criado, L. A. Pérez-Maqueda, C. Popescu, and N. Sbirrazzuoli, "ICTAC Kinetics Committee Recommendations for Performing Kinetic Computations on Thermal Analysis Data," *Thermochimica Acta* 520 (2011): 1–19, https://doi.org/10.1016/j.tca.2011.03.034.

26. W. Xing, G. Jie, L. Song, X. Wang, X. Lv, and Y. Hu, "Flame Retardancy and Thermal Properties of Epoxy Acrylate Resin/Alpha-Zirconium Phosphate Nanocomposites Used for UV-Curing Flame Retardant Films," *Materials Chemistry and Physics* 125 (2011): 196–201, https://doi.org/10.1016/j.matchemphys.2010.09.006.

27. M. Natarajan and S. C. Murugavel, "Thermal Stability and Thermal Degradation Kinetics of Bio-Based Epoxy Resins Derived From Cardanol by Thermogravimetric Analysis," *Polymer Bulletin* 74 (2017): 3319–3340, https://doi.org/10.1007/s00289-016-1885-y.

28. S. Yousef, J. Eimontas, N. Striūgas, M. Praspaliauskas, and M. A. Abdelnaby, "Pyrolysis Kinetic Behaviour of Glass Fibre-Reinforced Epoxy Resin Composites Using Linear and Nonlinear Isoconversional Methods," *Polymers* 13 (2021): 1–18, https://doi.org/10.3390/polym13101543.

29. A. R. Bahramian, M. Kokabi, and F. P. Soorbaghi, "Carbon Fiber Reinforced β-SiAlON for Ultra High Temperature Ablative Heat Shields," *International Journal of Applied Ceramic Technology* 10 (2013): 203–214, https://doi.org/10.1111/j.1744-7402.2012.02837.x.

30. R. Nayak, D. P. Tarkes, and A. Satapathy, "A Computational and Experimental Investigation on Thermal Conductivity of Particle Reinforced Epoxy Composites," *Computational Materials Science* 48 (2010): 576–581, https://doi.org/10.1016/j.commatsci.2010.02.025.

31. S. K. Moshir, S. V. Hoa, F. Shadmehri, D. Rosca, and A. Ahmed, "Mechanical Behavior of Thick Composite Tubes Under Four-Point Bending," *Composite Structures* 242 (2020): 112097, https://doi.org/10.1016/j.compstruct.2020.112097.

32. Products L, "Structural Design Analysis," 1991.

33. G. Nikolic, S. Zlatkovic, M. Cakic, S. Cakic, C. Lacnjevac, and Z. Rajic, "Fast Fourier Transform IR Characterization of Epoxy GY

Systems Crosslinked With Aliphatic and Cycloaliphatic EH Polyamine Adducts," *Sensors* 10 (2010): 684–696, https://doi.org/10.3390/s100100684.

34. D. Mamalis, T. Flanagan, and C. M. Ó Brádaigh, "Effect of Fibre Straightness and Sizing in Carbon Fibre Reinforced Powder Epoxy Composites," *Composites Part A: Applied Science and Manufacturing* 110 (2018): 93–105, https://doi.org/10.1016/j.compositesa.2018.04.013.

35. I. J. Fernandes, R. V. Santos, E. C. A. D. Santos, T. L. A. C. Rocha, N. S. Domingues, and C. A. M. Moraes, "Replacement of Commercial Silica by Rice Husk Ash in Epoxy Composites: A Comparative Analysis," *Materials Research* 21, no. 3 (2018): e20160562, https://doi.org/10.1590/1980-5373-MR-2016-0562.

36. L. Cheng, L. Zheng, G. Li, J. Zeng, and Q. Yin, "Influence of Particle Surface Properties on the Dielectric Behavior of Silica/Epoxy Nanocomposites," *Physica B: Condensed Matter* 403 (2008): 2584–2589, https://doi.org/10.1016/j.physb.2008.01.021.

37. A. Vinod, R. Vijay, D. Lenin Singaravelu, et al., "Effect of Alkali Treatment on Performance Characterization of *Ziziphus mauritiana* Fiber and Its Epoxy Composites," *Journal of Industrial Textiles* 51 (2022): 2444S–2466S, https://doi.org/10.1177/1528083720942614.

38. J. M. Antonucci and Æ. D. Skrtic, "Amorphous Calcium Phosphate/Urethane Methacrylate Resin Composites. I. Physicochemical Characterization," *Journal of Materials Science: Materials in Medicine* 19 (2008): 507–515, https://doi.org/10.1007/s10856-007-3178-3.

39. N. Hameed, P. A. Sreekumar, B. Francis, W. Yang, and S. Thomas, "Morphology, Dynamic Mechanical and Thermal Studies on Poly(Styrene-Co-Acrylonitrile) Modified Epoxy Resin/Glass Fibre Composites," *Composites Part A: Applied Science and Manufacturing* 38 (2007): 2422–2432, https://doi.org/10.1016/j.compositesa.2007.08.009.

40. J. Tarrío-Saavedra, J. López-Beceiro, S. Naya, and R. Artiaga, "Effect of Silica Content on Thermal Stability of Fumed Silica/Epoxy Composites," *Polymer Degradation and Stability* 93 (2008): 2133–2137, https://doi.org/10.1016/j.polymdegradstab.2008.08.006.

41. D. G. Cahill, S. K. Watson, and R. O. Pohl, "Lower Limit to the Thermal Conductivity of Disordered Crystals," *Physical Review B* 46 (1992): 6131–6140, https://doi.org/10.1103/PhysRevB.46.6131.

42. C. Kaynak, E. S. Erdiller, L. Parnas, and F. Senel, "Use of Split-Disk Tests for the Process Parameters of Filament Wound Epoxy Composite Tubes," *Polymer Testing* 24 (2005): 648–655, https://doi.org/10.1016/j.polymertesting.2005.03.012.

43. M. Liang, X. Liu, D. Liu, et al., "A Review of the Curing Rate and Mechanical Properties of Epoxy Resin on Polymer Matrix Composites," *Journal of Polymer Research* 31 (2024): 337, https://doi.org/10.1007/s10965-024-04186-y.

44. T. Üstün, V. Eskizeybek, and A. Avci, "Enhanced Fatigue Performances of Hybrid Nanoreinforced Filament Wound Carbon/Epoxy Composite Pipes," *Composite Structures* 150 (2016): 124–131, https://doi.org/10.1016/j.compstruct.2016.05.012.